Supporting Information

Water-mediated electro-hydrogenation of CO_2 at near-equilibrium potential by carbon nanotubes/cerium dioxide nanohybrids

Giovanni Valenti,[1‡] Michele Melchionna,[2‡] Tiziano Montini,[2] Alessandro Boni,[1] Lucia Nasi,[3] Emiliano Fonda,[4] Alejandro Criado,[5] Andrea Zitolo,[4] Silvia Voci,[1] Giovanni Bertoni, [3,6] Marcella Bonchio,*[7] Paolo Fornasiero,*[2,8] Francesco Paolucci,*[1,9] and Maurizio Prato*[2,5,10]

[1] Department of Chemistry "Giacomo Ciamician", University of Bologna, via Selmi 2, 40126 Bologna, Italy.

[2] Department of Chemical and Pharmaceutical Sciences, University of Trieste and Consortium INSTM, Via L. Giorgieri 1, 34127 Trieste, Italy.

[3] CNR-IMEM Institute, Parco area delle Scienze 37/A, 43124 Parma, Italy.

[4] Synchrotron SOLEIL,L'Orme des Merisiers, BP48 Saint Aubin, 91192 Gif-sur-Yvette, France

[5] Center for Cooperative Research in Biomaterials (CIC biomaGUNE), Basque Research and Technology Alliance (BRTA), Paseo de Miramón 182, 20014, Donostia San Sebastián, Spain

[6] CNR - Istituto Nanoscienze, Via Campi 213/A, 41125 Modena, Italy

[7] ITM-CNR, Consortium INSTM and Department of Chemical Sciences, University of Padova, Via F. Marzolo 1, 35131 Padova, Italy[8] ICCOM-CNR, University of Trieste, Via L. Giorgieri 1, 34127 Trieste, Italy.

[9] ICMATE-CNR Bologna Associate Unit, University of Bologna, via Selmi 2, 40126 Bologna, Italy

[10] Ikerbasque, Basque Foundation for Science, Bilbao, 48013, Spain

[‡] These authors contributed equally to this work

Corresponding Author

Marcella Bonchio marcella.bonchio@unipd.it
Paolo Fornasiero pfornasiero@units.it
Francesco Paolucci francesco.paolucci@unibo.it
Maurizio Prato prato@units.it

Table of Contents

Products Analysis

For the gas phase analysis, the saturating gas (Ar or CO_2) was continuously bubbled through the electrolyte and analyzed on-line using an Agilent 7890 gaschromatograph equipped with a 10-way valve for injection and 2 analytical lines. CO possibly produced has been analyzed using a Permanent Gas/CO_2 column (parallel columns MolSieve 5A 10m x 0.32 mmID and PoraPlot Q 60m x 0.53mm ID) with He as carrier and connected to a methanizer and a FID detector. H_2 has been monitored using a MolSieve 5A (30m x 0.53 mm) column using Ar as carrier and connected to a TCD detector.

Qualitative analysis of formed HCO_2^- has been performed by SPME-GC/MS analysis. A Supelco fibers coated with Carboxen/Polydimethylsiloxane (CAR/PDMS, thickness 75 μm) has been employed for SPME extraction. After preconditioning before the day's analyses, a new 1-cm CAR/PDMS fiber in a manual injection holder has been used for FA extraction by the static headspace method. During this step, the solution of HNO_3 0.1M after electrocatalytic reduction of CO_2 has been transferred into a 10 mL vial, sealed with a screw cap and heated at 50 °C. Adsorption of FA has been performed exposing the fiber for 15 min in the vial headspace. The adsorbed molecules have been desorbed by introducing the SPME fiber into the injector of a 7890 Agilent gaschromatograph, set at 270 °C in splitless mode for 2 min. FA has been analysed using a DB-522ms column (J&W, 60 m × 0.32 mm ID, 20 μm film), using He as carrier gas. The mass spectra of the eluted FA have been acquired using a 5975C Agilent mass spectrometer, connected at the end of the GC column. Quantification of formic acid from CO_2 reduction is detected by analysis of the liquid phase after prolonged electrolysis by Ionic Chromatography. After each electrolysis, small amounts of solution (2 mL) are extracted from the electrochemical cell and immediately analyzed. The pH of each aliquot has been corrected with H_2SO_4 following a standard procedure. The formic acid was quantified at the end of the electrolysis using a Metrohm 883 instrument equipped with a conductometric detector and a Metrosep A Supp5 250/4.0 column using a $NaHCO_3$ 1mM / Na_2CO_3 3.2 mM solution as mobile phase.

Transmission electron microscopy (TEM)

HRTEM and STEM in high-angle annular dark-field mode (HAADF) were performed on a JEOL JEM-2200FS microscope, working at 200 kV. The elemental maps for cerium and carbon (Figure 2B) were acquired with EDXS on the same microscope. In the STEM-HAADF images and tomography projections, an inner cutoff angle of the STEM detector >100 mrad was chosen, to reduce the contribution from coherent contrast to the minimum and to enhance chemical contrast. The 3D tomography reconstruction (Figure 1B) was obtained by weighted back projection (WBP) followed by simultaneous iterative reconstruction technique (SIRT) with 20 iterations from a series of 53 projections acquired from −40° to +64° with 2° tilt step. Energy-filtered imaging (EFTEM) was performed by using an in-column omega filter, for further chemical mapping of carbon, oxygen, and cerium (from the C-K ionization edge at 284 eV, O-K edge at 532 eV, and Ce-N edge at 110 eV, respectively).

Thermogravimetric analysis (TGA)

TGA of approximately 1 mg of each compound is recorded on a TGA Q500 (TA Instruments) under air, by equilibrating at 100 °C, and following a ramp of 10 °C min^{-1} up to 800 °C.

RAMAN spectroscopy

Raman spectra are recorded with an Invia Renishaw microspectrometer (50) equipped with He−Ne laser at 532 nm. To avoid sample damage or laser-induced heating/crystallization of the materials, the incident power was kept at 1 % (full power of the laser is 100 mV). Powders are dispersed in EtOH, drop-cast onto a quartz slide and the solvent evaporated; at least 5 spectra per sample are recorded on different areas of the sample in order to check the uniformity of the materials.

X-Ray photoelectron spectroscopy (XPS)

In order to validate the changes in the Ce surface valance chemistry, X-ray photoelectron spectroscopic (XPS) analysis was performed on bulk-CeO_2, nano-CeO_2 and CNT-CeO_2 at optimized conditions.[1-3] Figure 2 shows the deconvoluted XPS Ce 3d spectra. In this figure, v^0, v, u^0, and u peaks are the characteristic peaks of Ce^{3+}; while v, v'', v''', u, u'', and u''' are attributed to Ce^{4+} ions.

A semiquantitative analysis for the Ce^{3+} concentration can be provided by the *Equation S1* considering the integrated area of the different components of the fitted Ce 3d core level spectra:

$$[Ce3+] = \frac{Av0 + Av' + Au0 + Au'}{Av0 + Av' + Av'' + Av''' + Au0 + Au' + Au'' + Au'''} \qquad (S1)$$

Where *A* is the integrated area of peak (Table S1).

Table included in Figure 2 lists the peak position for all analyzed samples and the Ce^{3+} concentration. All analyzed samples showed a similar Ce^{3+} concentration.

XPS measurements were performed in a SPECS Sage HR 100 spectrometer with a non-monochromatic X ray source of Aluminum with a Kα line of 1486.6 eV energy and 300 W. The samples were placed perpendicular to the analyzer axis and calibrated using the 3d5/2 line of Ag with a full width at half maximum (FWHM) of 1.1 eV. An electron flood gun was used to compensate for charging during XPS data acquisition. The selected resolution was 30 and 15 eV of Pass Energy and 0.5 and 0.15 eV/step for the survey and high resolution spectra, respectively. All binding energies were referenced to the component Ce 3d 3/2 *u'''* 916.70 eV.[3] Fitting of the XPS data were done using CasaXPS 2.3.16 PR 1.6 software. For our data, the Shirley-type background subtraction was used and all curves were defined as 40% Lorentzian, 60% Gaussian. Atomic ratios were computed from experimental intensity ratios and normalized by atomic sensitivity factors.

X-Ray absorption spectroscopy (XAS)

MWCNT@CeO_2 powder has been grinded to fine powder and 10 mg have been mixed with 50 µl of deionized water and 50 µl of commercial 5 wt % Nafion perfluorinated resin solution (Merck). The suspension has been sonicated for 30 minutes; finally, a drop of 50 µl has been put on a Highly Oriented Pyrolytic Graphite (HOPG) window (Goodfellow cat. C 000200/2), and let dry at 60°C in air. The window has been installed on a PECC-2 photo-electrochemical cell from Zahner-elektrik Gmbh as used in previous experiments.[4-7] The cell was equipped with a Ag/AgCl reference electrode and it has been filled with HNO_3 0.1M in water. The solution has been bubbled with high purity Ar before and during the experiment. Measurement and control of potential has been achieved with a BioLogic Potentiostat. All X-ray absorption measurements have been performed at SAMBA (Synchrotron SOLEIL): Si 220 sagittaly

bent monochromator and two Pd mirrors set at 7.5 mrad incidence angle ensured monochromaticity of the beam and focusing, while IC-SPEC (FMB-Oxford) ionization chambers filled with a mixture of nitrogen and helium were used to monitor beam intensity, fluorescence detection has been performed with a pixelated (6x6) Ge detector (Mirion) with DxMap digital signal processors (XIA). Monochromator energy scale was calibrated versus a pure Cr foil (GoodFellow). EXAFS data analysis has been performed with the IFeffit[8] and Feff8.4[9] software.

Inductively coupled plasma-optical emission spectrometry (ICP-OES)

ICP-OES (Optical emission spectrometry) analysis was recorded on an Optima 8000 Perkinelmer instrument.

CO_2 absorption.

The absorption and interaction of CO_2 with **MWCNT@CeO_2** has been revealed by CVs and EIS, following the different behavior of surface capacitance in the presence or absence of CO_2 in solution. By scanning the potential at different scan rates (υ) in a region where only capacitive currents are present, e.g. no faradaic reactions occur, it is possible to determine the capacitance of the electrode from the slope of a current vs. υ plot, that is a capacitance by definition. CVs both in Ar- and CO_2-sat solutions were recorded in the potential range ±50 mV *vs.* OCP. The fittings give values of 4.1 mF cm^{-2} and 2.4 mF cm^{-2} when the solution is degassed with CO_2 or Ar respectively. Also, from EIS recorded at OCP, **MWCNT@CeO_2** displays a different response when CO_2 is dissolved in solution. From the Bode plot of Figure S9d is possible to see two different time constants in Ar-saturated solution that merge in a single one in the presence of CO_2. It is also possible to notice that the solution resistance (Log|Z| values at high frequencies) in a CO_2-sat solution increases by almost 50 Ohm (78 Ω vs. 123 Ω). This effect is probably caused by surface absorption of CO_2 molecules that increase electrode's resistivity.

Additionally, room temperature CO_2 chemisorption experiments were performed on a ASAP 2020C apparatus in the pressure range 10-800 Torr. Typically, 50 mg of samples were degassed at 150 °C for 12 h before the experiment.

Characterization in Phosphate Buffer

The redox activity of CeO_2 can be followed by CVs in 0.1M Phosphate Buffer (PB) solution (pH = 6.8). When Ce^{4+} is reduced to Ce^{3+} (equation S2) in the presence of phosphate anions, the slow chemical equilibrium of $CePO_4$ formation takes place. This phosphate specie can then be electrochemically re-oxidized and its related redox process (equation S3) appears in cyclic voltammetry, with $E_{1/2}$= +0.5V Ag/AgCl.

$$2\ CeO_{2\ (surface)} + 2\ e^- + 2\ H^+ \rightarrow Ce_2O_{3\ (surface)} + H_2O \qquad (S2)$$

$$Ce_3(PO_4)_{4\ (surface)} + 3\ e^- + 3\ H^+ \leftrightarrows 3\ CePO_{4\ (surface)} + H_3PO_4 \qquad (S3)$$

The occurrence of these surface processes, reported by Cummings *et al.* on CeO_2 nanoparticle films,[10] enable to determine the amount of electroactive CeO_2 present on the electrodes. This allows to obtain the turnover frequency for **MWCNT@CeO₂** (see later) after normalization of the detected formic acid by the quantity of electroactive catalyst. The voltammetric peaks with $E_{1/2}$= +0.5V Ag/AgCl reach a steady intensity after 15 cycles and their integration reveals a charge of both oxidation and reduction process of 43 μC. Considering the total amount of CeO_2 deposited on the electrode within the nanocomposite **MWCNT@CeO₂**, and the charge related to redox process A, we estimate that ~20% of the deposited CeO_2 is electrochemically active. The formation of this surface equilibrium involving phosphate anions is however a major drawback with respect to the electrochemical CO_2 conversion in this particular electrolyte. The voltammetric response of a CO_2-saturated 0.1M PB decreases with potential cycling, and after 20 cycles almost no faradaic current is observable anymore. Both $Ce^{4+/3+}$ reduction and CO_2 reduction occur in the scanned potential window, but after complete formation of surface $CePO_4$ also CO_2 reduction is suppressed.

Electrochemical characterization of CeO_2

Films of nanocrystalline **CeO_2** are prepared with the same procedure mentioned in the main text, adjusting the amount of the dropcast in a way that the same weight of oxide powder is deposited on the electrode. In this way is possible to directly compare the electrochemical behavior of **MWCNT@CeO₂** and **CeO_2**. Comparison of the CVs shows how the redox process at $E_{1/2}$= +0.5V Ag/AgCl disappears on **CeO_2** films,

and how the overall capacitive current is reduced in the latter case. The suppression of any faradaic current is somehow surprising but reveal the fundamental role of CNTs in transferring charge from the underlying glassy carbon (GC) electrode throughout the nanocomposite film and finally to the surface of CeO_2. With thick film of nanocrystalline CeO_2 is not possible to observe the redox process related to the formation of the surface specie $CePO_4$ (equation S3), while in the case of **MWCNT@CeO_2** the nanometric shell of ceria around CNTs is thin enough to enable charge transfer. The same characterization of CO_2 absorption detailed previously in HNO_3 0.1 M does not reveal any change in capacitive current after saturation of the solution with CO_2 instead that with Ar. Another peculiarity of **CeO_2** films is a general decrease of capacitive current, observed also with respect to a bare GC electrode. Therefore, the general reduction of capacitance is not solely related to a reduction of the electroactive area, but also reflects changes in the electronic properties of the oxide film. It is well known that layer of insulators (e.g. oxide, self-assembly monolayer, etc.) on top of metallic electrodes reduce the capacitive current. It is likely that thick films of un-doped nanocrystalline CeO_2 behave in this way reducing the surface capacitance by increasing the distance between the regions of excess charge.

Tafel plot.

The observed decrease in faradaic efficiency for HCOOH production at high overpotential is evidenced also by the change in slope in the Tafel plot. Data refer to steady-state chronoamperometry measurements. As long as concerned the potential region near the thermodynamic potential $E^{\mathbf{0}}$ [CO_2/FA], both methods are consistent and give the same slope. As the potential is made more cathodic, the change in slope reflects the transition between a kinetic limited region, with slope of 260mV dec^{-1}, where the production of formic acid is higher, to one with more facile kinetics, slope of 140 mV dec^{-1}, associated to a predominant hydrogen evolution reaction. In the low overpotential region multiple processes occur and participate together to CO_2 conversion (i.e. CeO_2 reduction, CO_2 absorption, proton absorption), resulting in a high Tafel slope, that also strongly depends on the state of the electrode surface and on the presence of surface redox couples (i.e. $Ce^{4+/3+}$) and functional groups. For this reason, we corrected the current density for the FE in order to consider only the contribution due to the CO_2RR. In the "high overpotential" region

hydrogen evolution becomes the dominant process: the corresponding Tafel slope of 140mV dec^{-1}, suggests several possible rate-limiting steps with kinetics possibly limited by a slow Volmer adsorption step ($H^+ + e^- \rightarrow H_{ads}$), plausible with the competition between H_{ads} and $CO_{2\ ads}$ for same sites on the oxide surface.

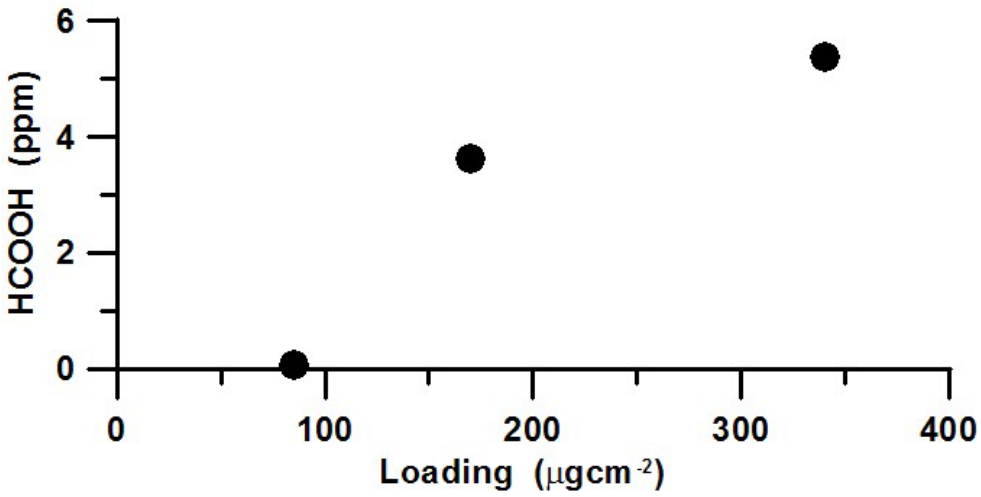

Figure S1. Catalyst loading optimization for CO_2RR performances. Formic acid production as a function of the nanocomposite different amounts. Overpotential (η), where η = -0.02 V. **MWCNT@CeO_2:** 85 μg cm^{-2}, 170 μg cm^{-2}, 340 μg cm^{-2}.

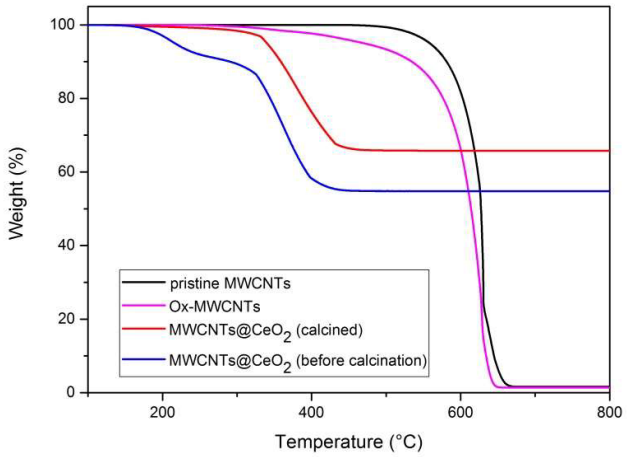

Figure S2. Effects of calcination on TGA. TGA profiles recorded under air flow of the fresh and calcined nanocomposites with and without the CeO_2.

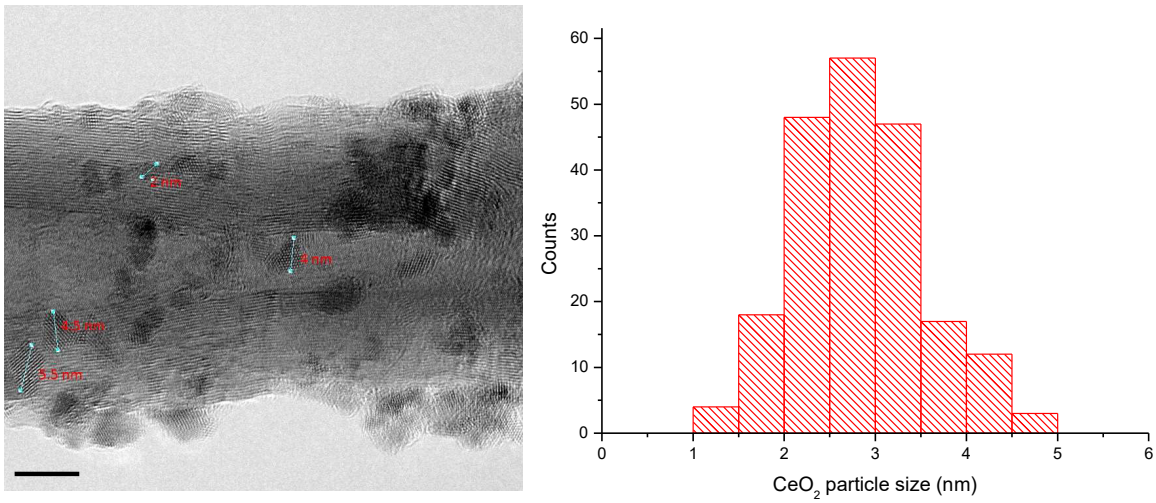

Figure S3. HRTEM of a MWCNT@CeO_2 and particle size analysis of the MWCNT@CeO_2

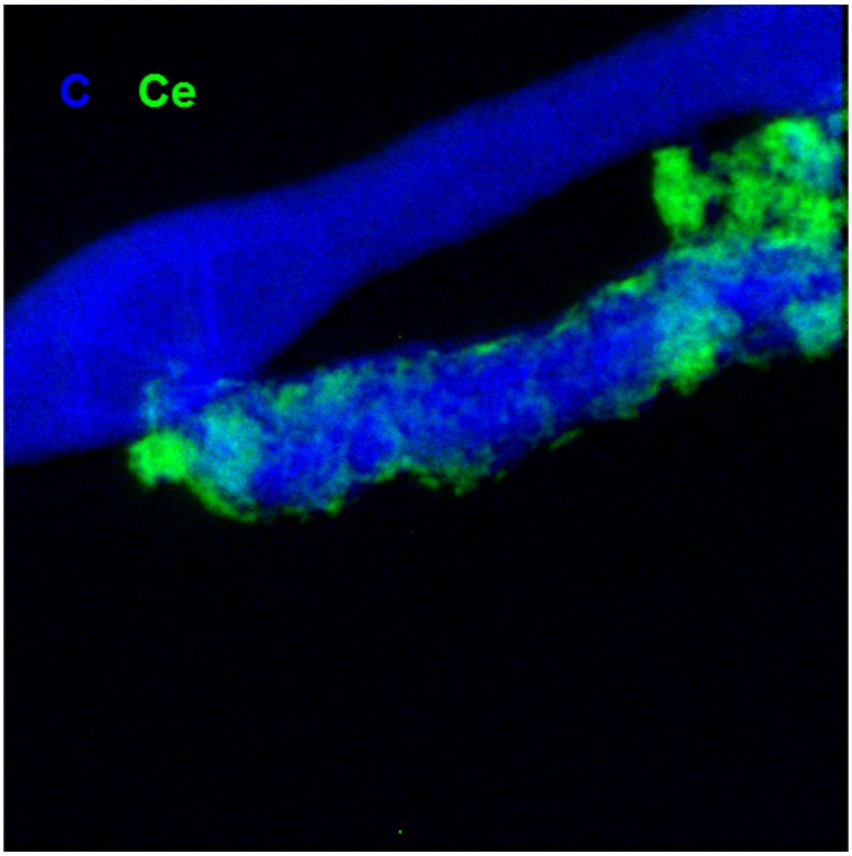

Figure S4. Energy-filtered transmission electron microscopy (EFTEM) of the MWCNT@CeO_2 showing the Ce (green) and the structure of MWCNT (blue).

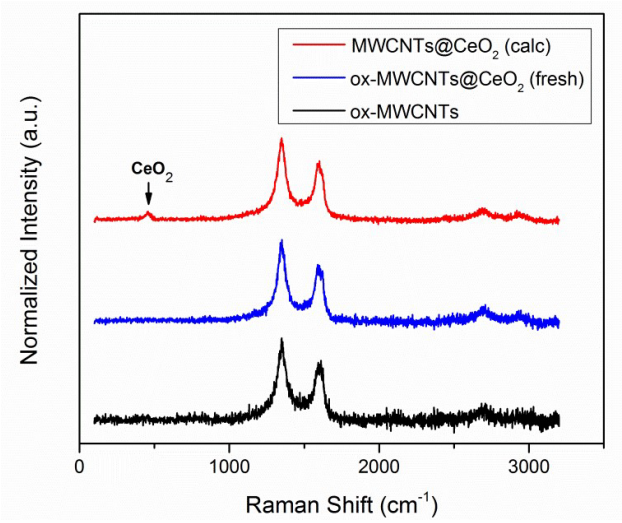

Figure S5. Raman spectra of the nanohybrids. Raman spectra of ox-MWCNTs, ox-MWCNTs@CeO_2 fresh and MWCNTs@CeO_2 calcined.

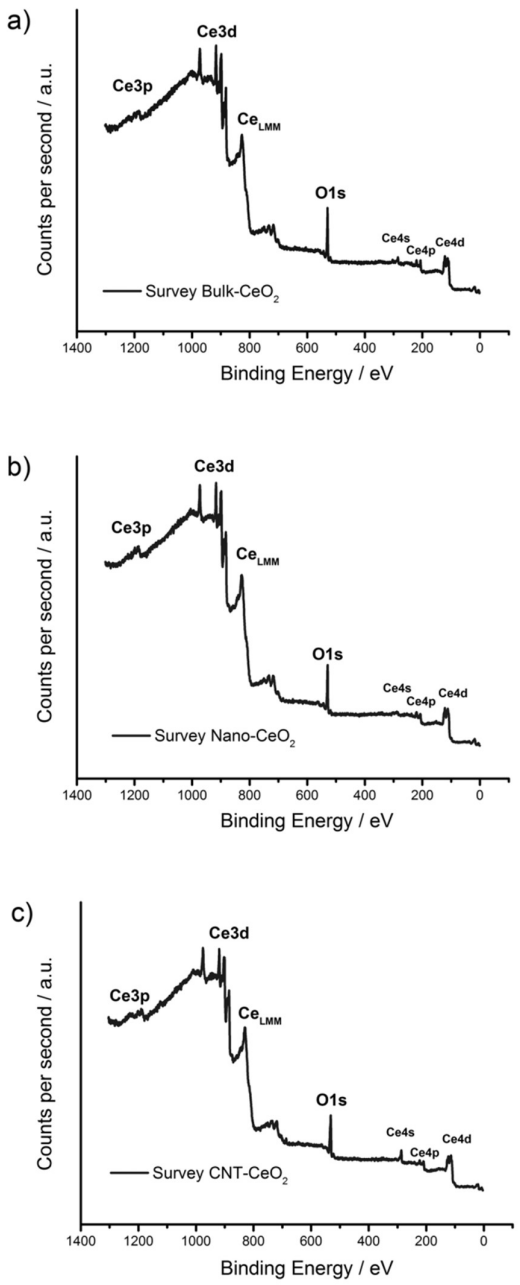

Figure S6. XPS survey of the materials. Survey spectra for (a) bulk-CeO_2, (b) CeO_2 NPs and (c) MWCNT-CeO_2.

Table S1. XPS Integrated area of peak individual components of the Ce 3d spectra for the different Ce-based samples.

Sample	Component	Position (eV)	FWHM	% Area.
bulk-CeO_2	Ce 3d 5/2 v	882.49	2.696	21.93
	Ce 3d 3/2 u	901.07	2.055	10.36
	Ce 3d 5/2 v''	888.32	4.878	15.26
	Ce 3d 3/2 u''	907.46	4.497	7.05
	Ce 3d 5/2 v'''	898.35	2.638	20.6
	Ce 3d 3/2 u'''	916.7	2.628	14.25
	Ce 3d 5/2 v'	884.89	2.7	4.51
	Ce 3d 3/2 u'	903.19	2.7	3.02
	Ce 3d 5/2 v0	879.72	2.88	1.81
	Ce 3d 3/2 u0	898.4	2.88	1.21
CeO_2-NPs	Ce 3d 5/2 v	882.19	2.024	12.39
	Ce 3d 3/2 u	900.71	2.024	8.3
	Ce 3d 5/2 v''	888.4	4.508	13.91
	Ce 3d 3/2 u''	907.44	5	9.32
	Ce 3d 5/2 v'''	898.2	2.752	18.36
	Ce 3d 3/2 u'''	916.7	2.752	12.3
	Ce 3d 5/2 v'	884.13	3.2	13.08
	Ce 3d 3/2 u'	902.28	3.4	8.76
	Ce 3d 5/2 v0	880.37	1.925	2.15
	Ce 3d 3/2 u0	898.5	1.925	1.44
MWCNT@CeO_2	Ce 3d 5/2 v	882.06	1.993	9.51
	Ce 3d 3/2 u	900.65	1.993	6.37
	Ce 3d 5/2 v''	888	4.81	14.25
	Ce 3d 3/2 u''	907.1	5.5	9.55
	Ce 3d 5/2 v'''	898.15	2.715	16.2
	Ce 3d 3/2 u'''	916.7	2.715	10.85
	Ce 3d 5/2 v'	883.88	3.8	17.77
	Ce 3d 3/2 u'	902.1	3.8	11.91
	Ce 3d 5/2 v0	880.19	2.353	2.16
	Ce 3d 3/2 u0	899	2.353	1.45

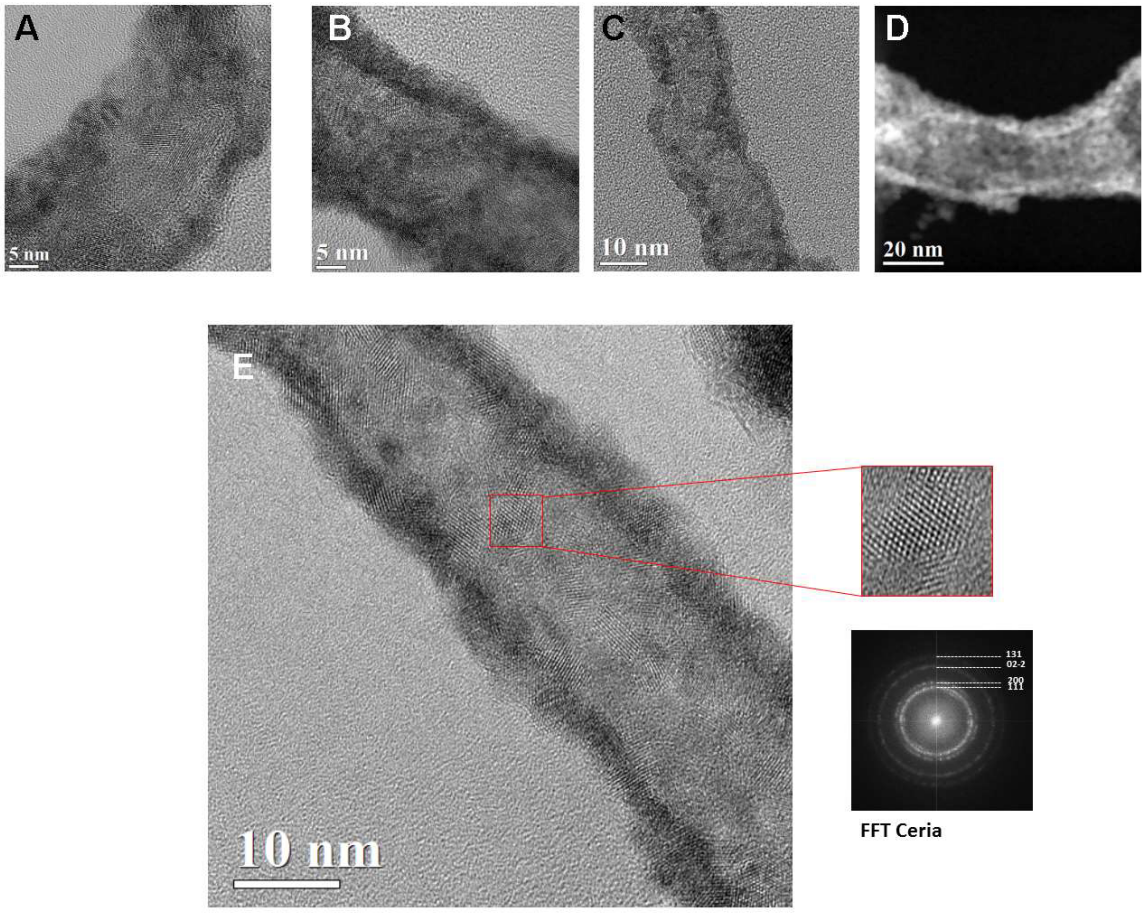

Figure S7. Recovered catalyst. Top: Representative TEM (A, B and C) and STEM-HAADF (D) micrographs of the recovered MWCNT@CeO_2 after electrolysis; bottom: HRTEM of the nanocomposite, with higher magnification of an area showing crystalline CeO_2 nanoparticle with the corresponding Fast Fourier Transform (FFT) indexed to crystalline CeO_2.

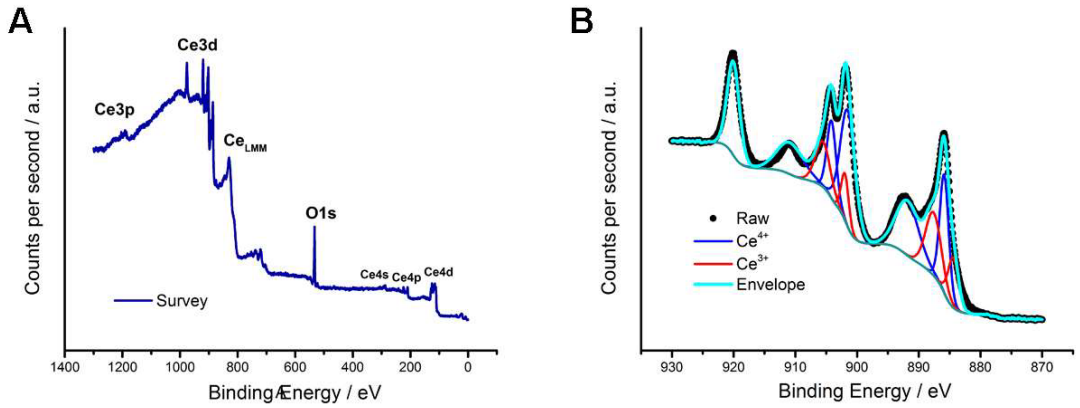

Figure S8. Post-catalysis XPS of the recovered catalyst. A) Survey spectrum of the recovered MWCNT@CeO_2 catalyst; B) Fitted XPS spectrum of Ce 3d core level.

Table S2. XPS Integrated area of peak individual components of the Ce 3d spectra for post-catalysis MWCNT@CeO_2.

Sample	Ce 3d $_{5/2}$ (eV)					Ce 3d $_{3/2}$ (eV)					[Ce^{3+}]
	v^0	v	v'	v''	v'''	u^0	u	u'	u''	u'''	
MWCNT@CeO_2 (post-catalysis)	881.05	882.52	884.25	888.32	898.15	898.62	900.79	902.18	907.51	916.7	**0.27**

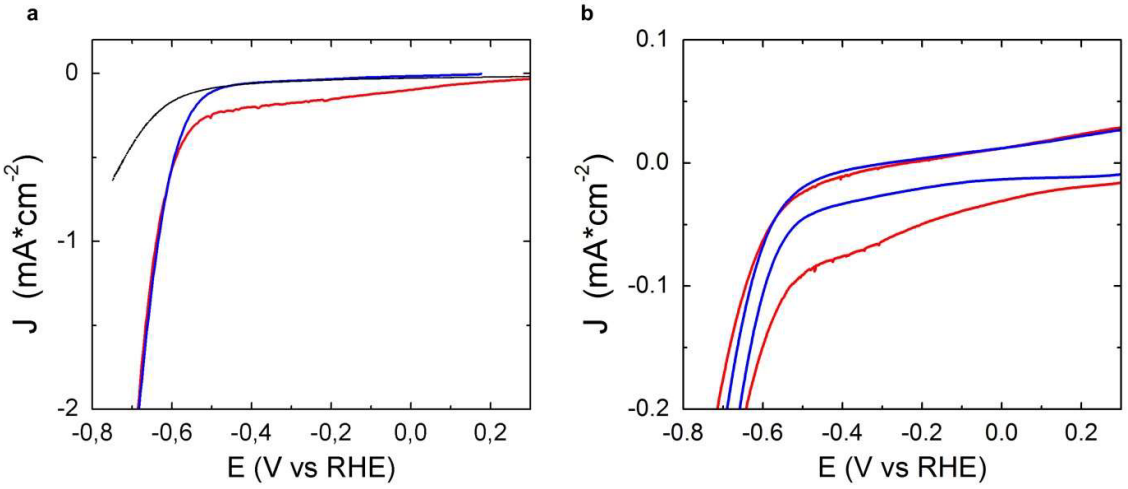

Figure S9. LSV at 2 mV s^{-1} (a) and CV at 50 mV s^{-1} (b) for the nanostructured catalyst **MWCNT@CeO_2** in a CO_2-saturated (red signal), Ar-saturated (blue signal) and **ox-MWCNT** in a CO_2-saturated (black signal) electrolyte solution. Electrolyte: HNO_3 0.1 M. Potentials are reported vs. RHE and are corrected for the uncompensated resistance.

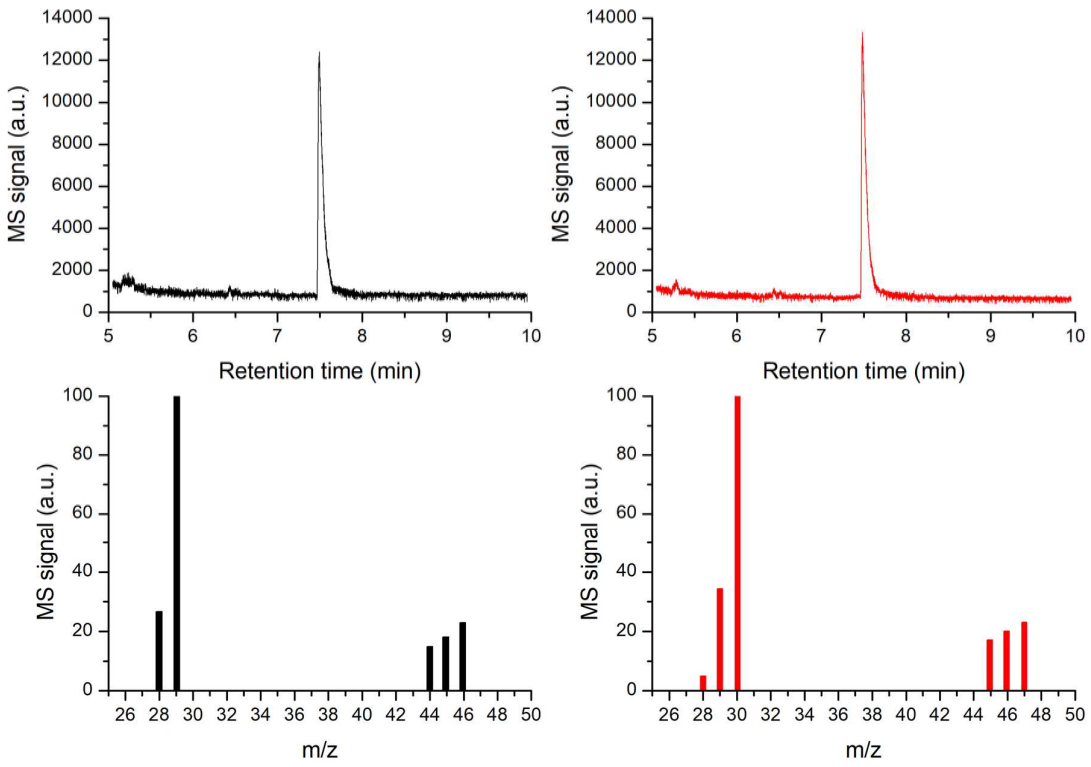

Figure S10. $^{13}CO_2$ isotope labelling mass spectrometry. A solid-phase microextraction followed by gas chromatography-mass spectrometry (SPME-GC/MS) method was used for qualitative analyze the FA formed from the CO_2RR using isotope labelled CO_2 (see Products Analysis description for more details). Gas chromatogram and corresponding mass spectrum of the electrolyte after chronoamperometry (at -0.22 V vs RHE for 1 h) under $^{12}CO_2$ (black) and $^{13}CO_2$ (red)-saturated electrolyte solution.

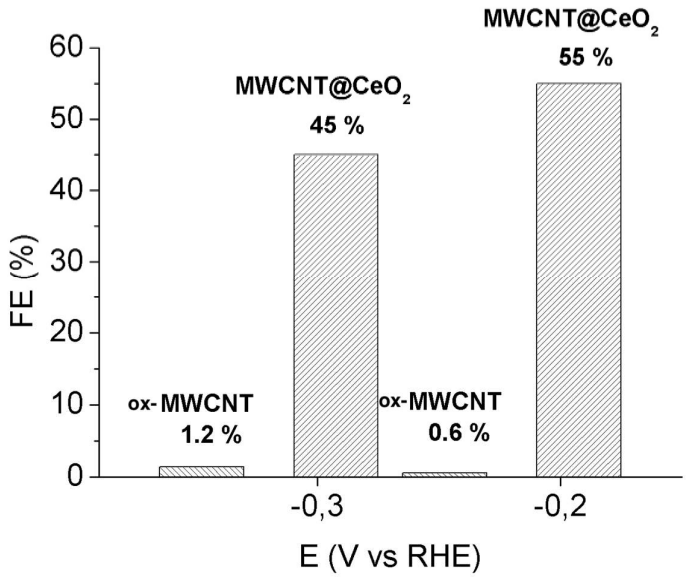

Figure S11. Faradaic Efficiency of **MWCNT@CeO₂** and **ox-MWCNT** for FA production in CO_2 at the two different potentials of -0.3 V and -0.2 V. Electrolyte: HNO_3 0.1 M. Potentials are reported vs. RHE and are corrected for the uncompensated resistance.

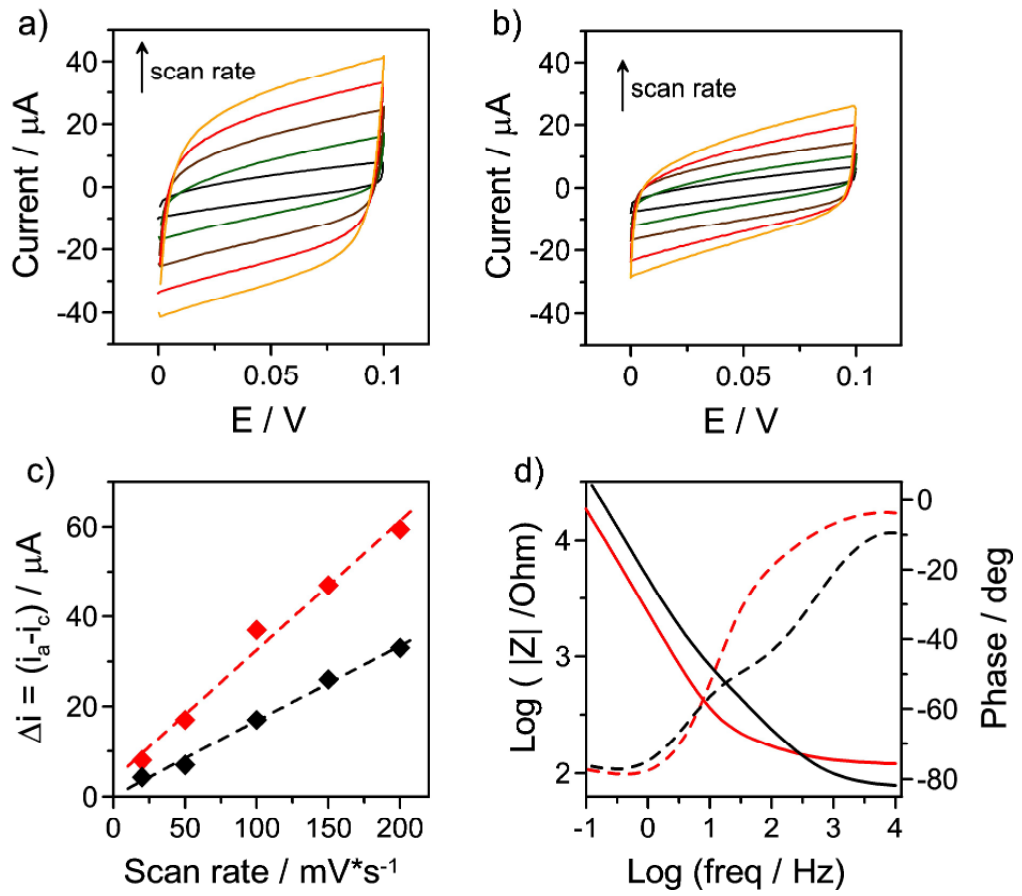

Figure S12. Representative CVs of **MWCNT@CeO₂** in a) CO_2-sat. and b) Ar-sat. HNO_3 0.1M solution. CVs were recorded in the potential range +/- 50 mV *vs.* OCP at a scan rate of 20, 50 100, 150 and 200 mV s^{-1}. Potential are reported vs. Ag/AgCl. c) Capacitive currents as a function of the scan rate, calculated as $\Delta i = (i_a - i_c)$ from CVs in a) and b). CO_2 (red) or argon (black) saturated solution. d) Impedance spectra (Bode plot) for MWCNT@CeO_2 at OCP in CO_2 (red) or Ar (black) saturated solution. Dashed lines refer to variations in the phase angle, while changes in the real component of impedance are displayed by the continue lines. Electrolyte: HNO_3 0.1 M.

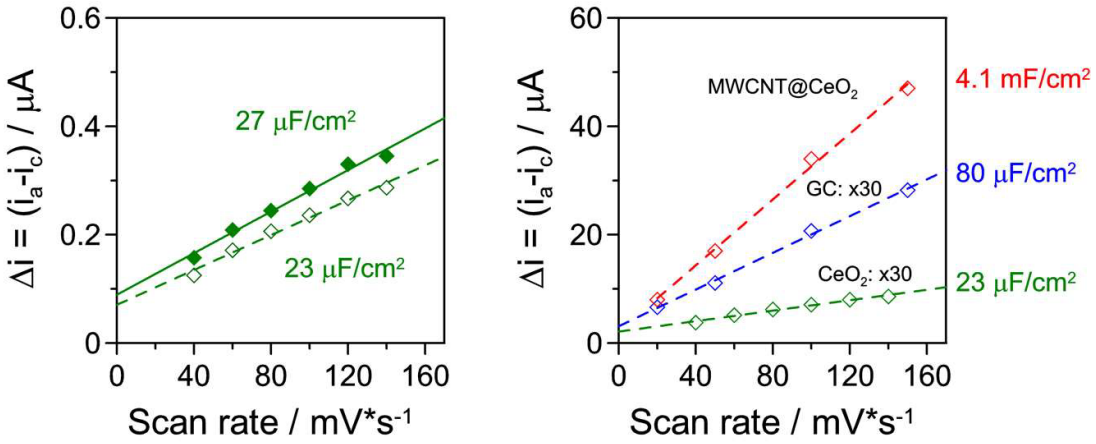

Figure S13. Capacitive currents for CeO_2 in CO_2- (green empty diamonds) and Ar- (green filled diamonds) saturated HNO_3 solutions as a function of the scan rate (*left*). right: capacitive currents for CeO_2 (green), bare GC electrode (blue) and MWCNT@CeO_2 (red) (*right*). Electrolyte: HNO_3 0.1 M.

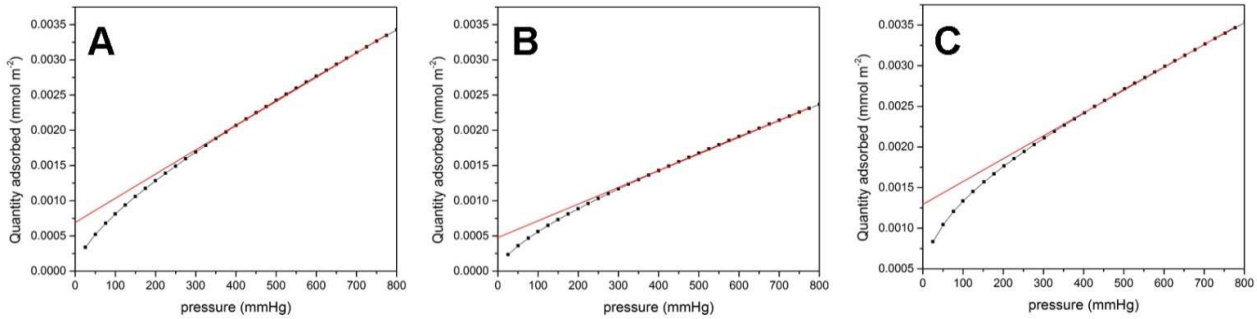

Figure S14. Room Temperature CO_2 chemisorption measurements for: A) CeO_2, B) MWCNT and C) MWCNT@CeO_2.

Table S3. Values of the CO_2 adsorbed quantities normalized by surface area for the three samples calculated by extrapolating the linear part of the isotherm to p = 0 atm.

Sample	CO_2 adsorbed
CeO_2	0.0007
MWCNT	0.0005
MWCNT/CeO_2	0.0013

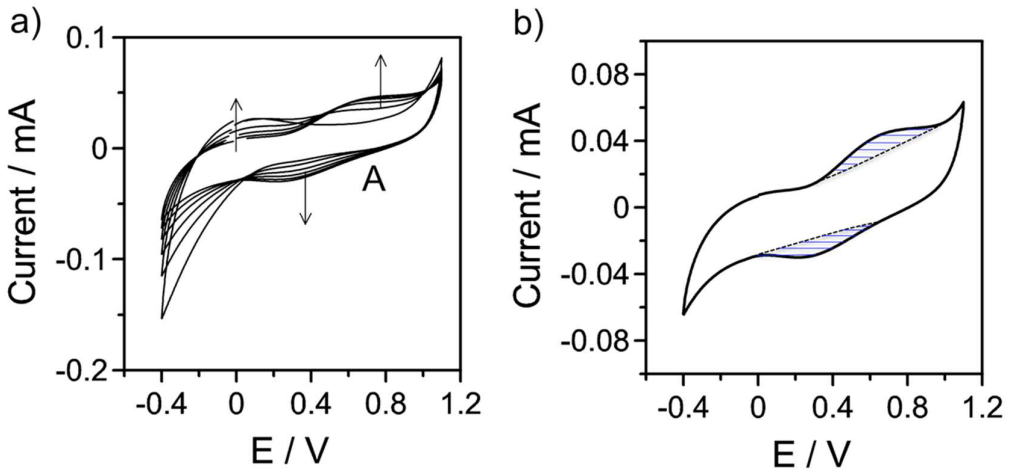

Figure S15. a) CVs in Phosphate Buffer of MWCNT@CeO_2. Scans n° 1-4-7-10-13-16 are plotted. b) The 16th cycle is plotted, with highlighted the charge related to the process of eq. 3. Potential are reported vs. Ag/AgCl sat. Scan rate = 50mV s^{-1}, PB 0.1M, pH=6.8.

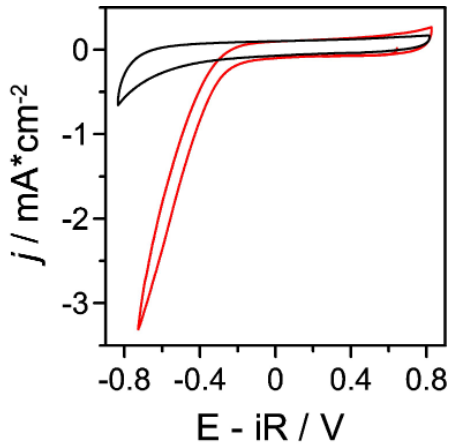

Figure S16. 1st (red line) and 20th (black line) CV scans of **MWCNT@CeO_2** in PB 0.1 M, scan rate 50mV s^{-1}. Potential are reported *vs.* RHE.

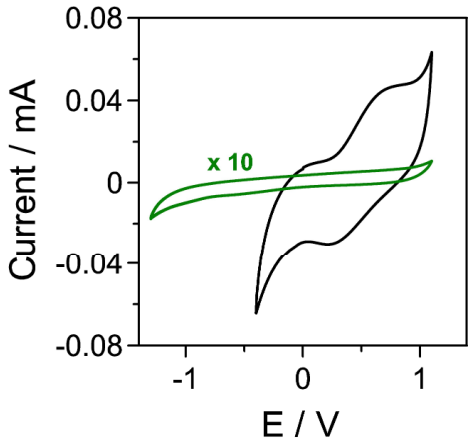

Figure S17. comparison between **MWCNT@CeO_2** (black curve) and CeO_2 (green curve) behavior in Phosphate Buffer. Scan rate = 50mV s^{-1}, PB 0.1M, pH=6.8.

Table S4: formic acid detection with ionic chromatography after electrolysis for **MWCNT@CeO_2**. The mean value of two subsequent analysis, converted to concentration of formic acid, has been used for the calculation of faradaic efficiency and turnover frequency. Potentials are reported vs. RHE.

	Analysis #1 / ppm	**Analysis #2 / ppm**
# 1 (E= -0.22V)	3.041	3.085
# 3 (E= -0.32V)	2.872	2.891
# 2 (E= -0.42V)	2.137	2.133
# 4 (E= -0.52V)	0.335	0.258

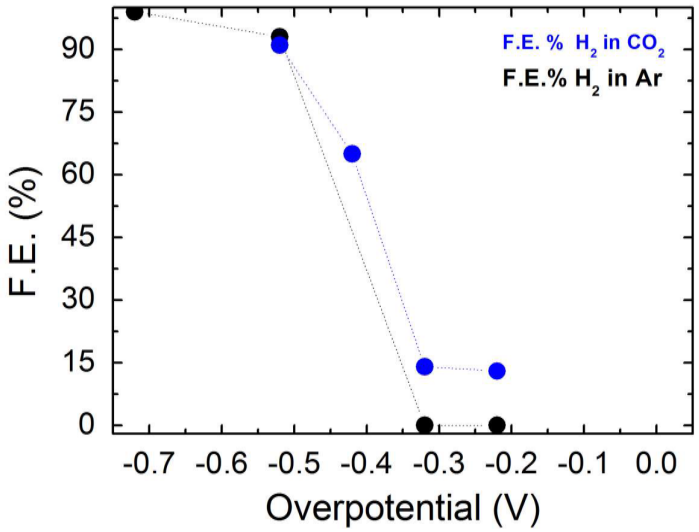

Figure S18. Faradaic Efficiency of **MWCNT@CeO_2** for H_2 production in CO_2 (blue) and Ar (black) saturated solution as a function of the potentials. Electrolyte: HNO_3 0.1 M

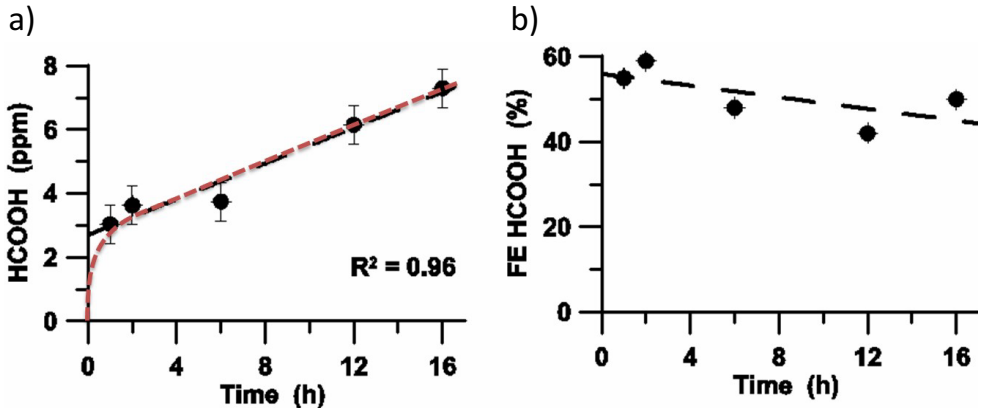

Figure S19. Stability of the nanohybrids. (a) Formic acid production and (b) FE as a function of the time. Overpotential (η) = -0.02 V. Time chosen t= 1, 2, 6, 12, 16 h. **MWCNT@CeO_2:** 85 μg cm^{-2}, 170 μg cm^{-2}, 340 μg cm^{-2}.

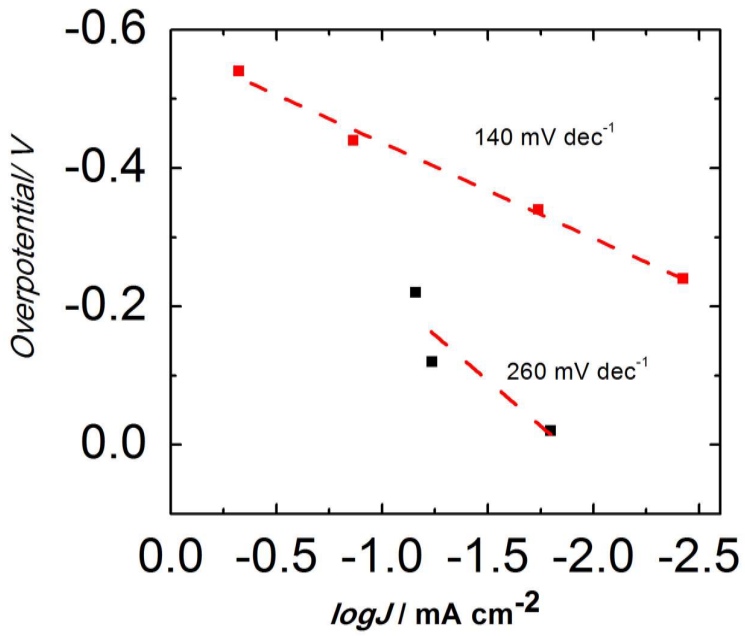

Figure S20. Tafel plot for **MWCNT@CeO_2** extracted from the CA data of Figure 4c. Red dots refers to current data obtained for HER by correcting the current density for the HER FE and the corresponded overpotential is related to the E' $_{HER}$ ($\eta = E_{app}$-E' [H_2/H^+], where E' [$H_2/H+$] = 0V RHE.) Black dots refers to current data obtained for CO_2RR by correcting the current density for the CO_2RR FE and the corresponded overpotential is related to the E' [CO_2/HCO_2H] ($\eta = E_{app}$-E' [CO_2/HCO_2H], where E' [CO_2/HCO_2H] = -0.2V RHE.) Electrolyte: HNO_3 0.1M.

Table S5. Comparison between the electrochemical performances of the nanohybrids **MWCNT@CeO_2** with other recently reported, highly active for the production of FA, CO_2RR.

Catalyst	Overpotential (V)	FE (%) for FA	Reference
MWCNT@CeO_2	**0.02**	**65**	**This work**
Cu-S	0.5	80	[11]
Sn/SnO_2	0.7	19	[12]
SnO_2	0.765	69	[13]
Sb	0.245	30	[14]
Co oxide	0.229	85	[15]
PdPt NPS	0.065	20	[16]
Pd NPS	0.207	97	[17]
AuPd	0.845	10	[18]
PdNP@CNHs	0.1	40	[19]
N-doped CNT	0.985	85	[20]
NP@SnO_2	0.88	61	[21]
NW@ SnO_2	0.78	87	[21]
Sn@MHKTs	0.78	95	[22]
Bi@MHKTs	0.78	92	[22]
Pb@MHKTs	0.78	85	[22]
$SnSe_2$@carbon cloth	0.54	88	[23]
Bi nanosheet	0.55	95.9	[24]

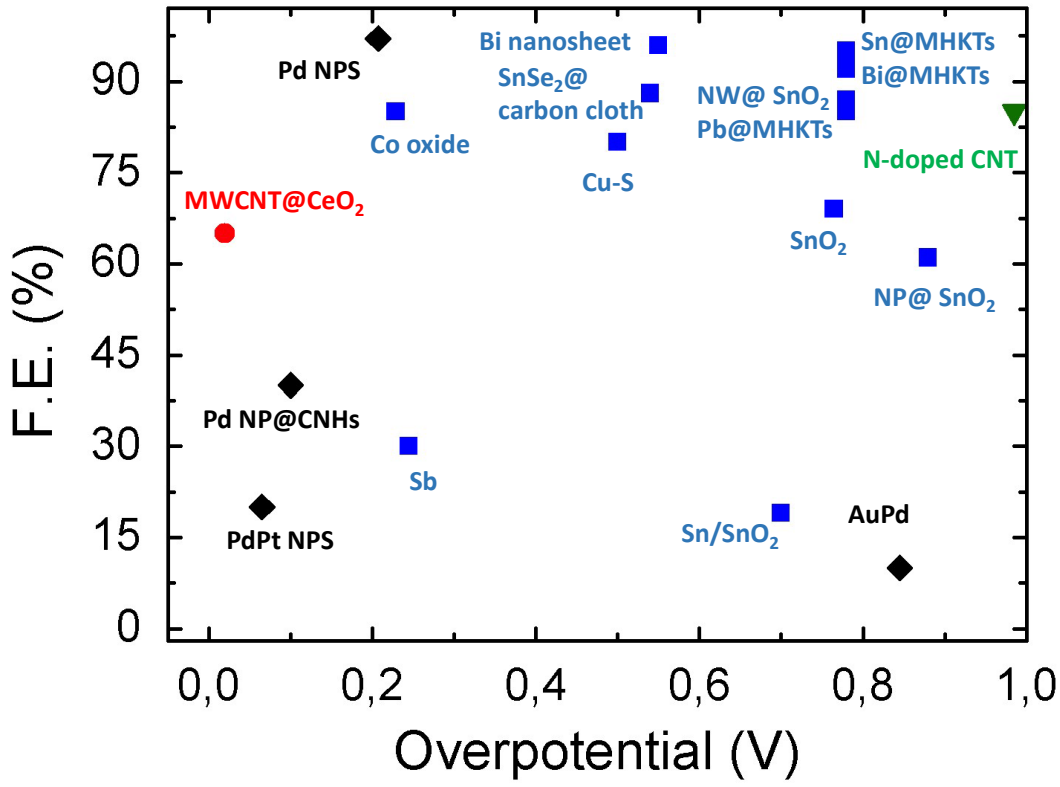

Figure S21. Direct comparison of FE for $HCOO^-$ generation for **MWCNT@CeO₂** nanohybrid (red dot) together with other recently reported heterogeneous electrocatalysts. Faradaic Efficiency of **MWCNT@CeO₂** for formic acid production at -0.02 overpotential (η) ($\eta = E_{app} - E°\ [CO_2/HCO_2H] - i_s \times R$, where E_{app} is the potential applied to the catalyst substrate corrected for the uncompensated resistance and $E°\ [CO_2/HCO_2H] = -0.2\ V_{RHE}$). The data are adapted from: for catalyst based on p-metals (blue squares) ref. 11 Cu-S (2018), ref. 12 Sn/SnO_2 (2012), ref. 13 SnO_2 (2015), ref. 14 Sb (2015), ref. 15 Co oxide (2016), ref 21 NP@SnO_2 (2020), ref 21 NW@SnO_2 (2020), ref 22 Sn@MHKTs (2019), ref 22 Bi@MHKTs (2019), ref 22 Pb@MHKTs (2019), ref 23$SnSe_2$@carbon cloth (2019), ref 24 Bi nanosheet (2019); for catalyst based on d-metals (black diamonds) ref. 16 PdPt NPS (2015), ref. 17 Pd NPS (2016), ref. 18 AuPd (2015), ref. 19 PdNP@CNHs (2018); for carbon-based catalyst (green triangle) ref. 20 N-doped CNT (2014).

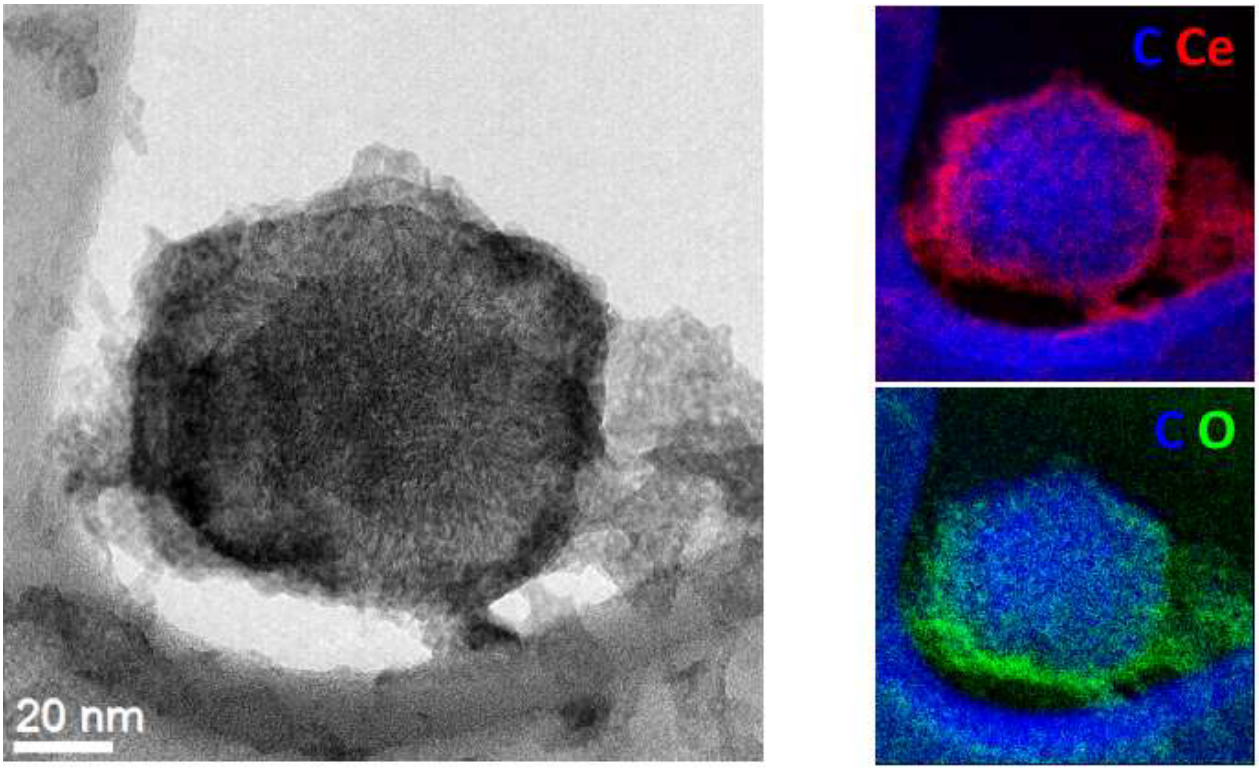

Figure S22. HRTEM (left) and corresponding EFTEM of a typical CNH@CeO_2 nanohybrid particle. The EFTEM confirms the achieved interface between the carbon and the metal oxide.

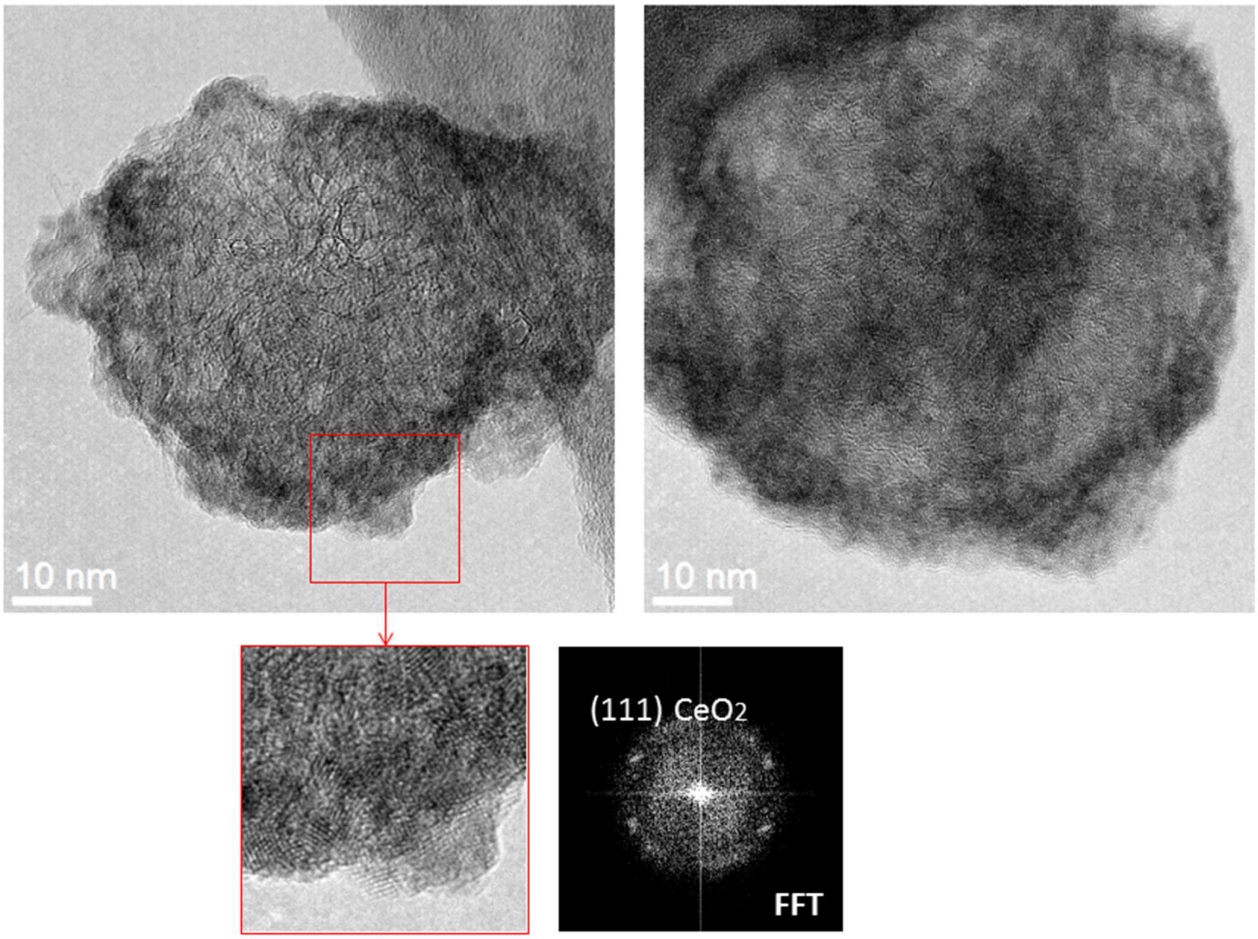

Figure S23. HRTEM and corresponding Fast Fourier Transform (FFT) in a selected area of the nanohybrid, confirming the layering of crystalline CeO_2 on the carbon scaffold.

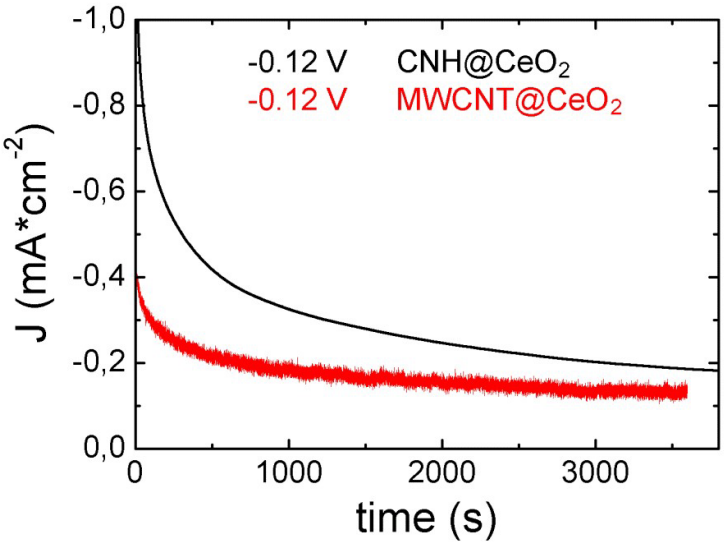

Figure S24. Chronoamperometry for the nanostructured catalysts MWCNT@CeO_2 (red line) and CNH@CeO_2 in HNO_3 0.1 M at an overpotential of -0.12 V.

References

1 Deshpande, S., Patil, S., Kuchibhatla, S. V. & Seal, S. Size dependency variation in lattice parameter and valency states in nanocrystalline cerium oxide. *Appl. Phys. Lett.* **87**, 133113, doi:10.1063/1.2061873 (2005).

2 Janoš, P. *et al.* Nanocrystalline cerium oxide prepared from a carbonate precursor and its ability to breakdown biologically relevant organophosphates. *Environ. Sci.: Nano* **4**, 1283-1293, doi:10.1039/C7EN00119C (2017).

3 Romeo, M., Bak, K., El Fallah, J., Le Normand, F. & Hilaire, L. XPS Study of the reduction of cerium dioxide. *Surf. Interface Anal.* **20**, 508-512, doi:10.1002/sia.740200604 (1993).

4 Zitolo, A. *et al.* Identification of catalytic sites in cobalt-nitrogen-carbon materials for the oxygen reduction reaction. *Nat. Commun.* **8**, 957, doi:10.1038/s41467-017-01100-7 (2017).

5 Karapinar, D. *et al.* Electroreduction of CO_2 on Single-Site Copper-Nitrogen-Doped Carbon Material: Selective Formation of Ethanol and Reversible Restructuration of the Metal Sites. *Angew. Chem. Int. Ed.* **58**, 15098-15103, doi:10.1002/anie.201907994 (2019).

6 Santori, P. G. *et al.* Effect of Pyrolysis Atmosphere and Electrolyte pH on the Oxygen Reduction Activity, Stability and Spectroscopic Signature of FeN_x Moieties in Fe-N-C Catalysts. *J. Electrochem. Soc.* **166**, F3311-F3320, doi:10.1149/2.0371907jes (2019).

7 Li, J. *et al.* Volcano Trend in Electrocatalytic CO_2 Reduction Activity over Atomically Dispersed Metal Sites on Nitrogen-Doped Carbon. *ACS Catal.* **9**, 10426-10439, doi:10.1021/acscatal.9b02594 (2019).

8 Ravel, B. & Newville, M. ATHENA, ARTEMIS, HEPHAESTUS: data analysis for X-ray absorption spectroscopy using IFEFFIT. *J. Synchrotron Rad.* **12**, 537-541, doi:doi:10.1107/S0909049505012719 (2005).

9 Ankudinov, A. L., Ravel, B., Rehr, J. J. & Conradson, S. D. Real-space multiple-scattering calculation and interpretation of x-ray-absorption near-edge structure. *Phys. Rev. B* **58**, 7565-7576, doi:10.1103/PhysRevB.58.7565 (1998).

10 Cummings, C. Y. *et al.* Underpotential surface reduction of mesoporous CeO_2 nanoparticle films. *J. Solid State Electr.* **12**, 1541-1548, doi:10.1007/s10008-008-0508-4 (2008).

11 Shinagawa, T., Larrazábal, G. O., Martín, A. J., Krumeich, F. & Pérez-Ramírez, J. Sulfur-Modified Copper Catalysts for the Electrochemical Reduction of Carbon Dioxide to Formate. *ACS Catal.* **8**, 837-844, doi:10.1021/acscatal.7b03161 (2018).

12 Chen, Y. & Kanan, M. W. Tin Oxide Dependence of the CO_2 Reduction Efficiency on Tin Electrodes and Enhanced Activity for Tin/Tin Oxide Thin-Film Catalysts. *J. Am. Chem. Soc.* **134**, 1986-1989, doi:10.1021/ja2108799 (2012).

13 Lee, S., Ocon, J. D., Son, Y.-i. & Lee, J. Alkaline CO_2 Electrolysis toward Selective and Continuous HCOO– Production over SnO2 Nanocatalysts. *J. Phys. Chem. C* **119**, 4884-4890, doi:10.1021/jp512436w (2015).

14 Medina-Ramos, J., Pupillo, R. C., Keane, T. P., DiMeglio, J. L. & Rosenthal, J. Efficient Conversion of CO_2 to CO Using Tin and Other Inexpensive and Easily Prepared Post-Transition Metal Catalysts. *J. Am. Chem. Soc.* **137**, 5021-5027, doi:10.1021/ja5121088 (2015).

15 Gao, S. *et al.* Partially oxidized atomic cobalt layers for carbon dioxide electroreduction to liquid fuel. *Nature* **529**, 68, doi:10.1038/nature16455 (2016).

16 Kortlever, R., Peters, I., Koper, S. & Koper, M. T. M. Electrochemical CO_2 Reduction to Formic Acid at Low Overpotential and with High Faradaic Efficiency on Carbon-Supported Bimetallic Pd–Pt Nanoparticles. *ACS Catal.* **5**, 3916-3923, doi:10.1021/acscatal.5b00602 (2015).

17 Klinkova, A. *et al.* Rational Design of Efficient Palladium Catalysts for Electroreduction of Carbon Dioxide to Formate. *ACS Catal.* **6**, 8115-8120, doi:10.1021/acscatal.6b01719 (2016).

18 Hahn, C. *et al.* Synthesis of thin film AuPd alloys and their investigation for electrocatalytic CO_2 reduction. *J. Mater. Chem. A* **3**, 20185-20194, doi:10.1039/C5TA04863J (2015).

19 Melchionna, M. *et al.* Pd@TiO_2/carbon nanohorn electrocatalysts: reversible CO_2 hydrogenation to formic acid. *Energy Environ. Sci.*, doi:10.1039/C7EE03361C (2018).

20 Zhang, S. *et al.* Polyethylenimine-Enhanced Electrocatalytic Reduction of CO_2 to Formate at Nitrogen-Doped Carbon Nanomaterials. *J. Am. Chem. Soc.* **136**, 7845-7848, doi:10.1021/ja5031529 (2014).

21 Chen, Z. *et al.* Wavy SnO_2 catalyzed simultaneous reinforcement of carbon dioxide adsorption and activation towards electrochemical conversion of CO_2 to HCOOH. *Appl. Catal. B: Environmental* **261**, 118243, doi:10.1016/j.apcatb.2019.118243 (2020).

22 Huang, J., Guo, X., Huang, X. & Wang, L. Metal (Sn, Bi, Pb, Cd) in-situ anchored on mesoporous hollow kapok-tubes for outstanding electrocatalytic CO_2 reduction to formate. *Electrochim. Acta* **325**, 134923, doi:10.1016/j.electacta.2019.134923 (2019).

23 Diao, Y. *et al.* Converting Rust to PEDOT Nanofibers for Supercapacitors. *ACS Appl. Energy Mater.* **2**, 3435-3444, doi:10.1021/acsaem.9b00244 (2019).

24 Wu, D. *et al.* Electrochemical Transformation of Facet-Controlled BiOI into Mesoporous Bismuth Nanosheets for Selective Electrocatalytic Reduction of CO_2 to Formic Acid. *ChemSusChem* **12**, 4700-4707, doi:10.1002/cssc.201901724 (2019).